

Fabrication of perovskite-type oxide $\text{La}_{0.5}\text{Pb}_{0.5}\text{MnO}_3$ nanoparticles and its dye removal performance

Haman Tavakkoli · Tahereh Moayedipour

Received: 6 February 2014 / Accepted: 13 June 2014 / Published online: 24 July 2014
© The Author(s) 2014. This article is published with open access at Springerlink.com

Abstract $\text{La}_{0.5}\text{Pb}_{0.5}\text{MnO}_3$ perovskite-type oxide is prepared by sol–gel method. The physical and chemical properties of a nanoparticle were characterized by differential thermal analysis (DTA), thermogravimetric analysis, XRD, and scanning electron microscopy (SEM) techniques. The adsorption effect of the sample is evaluated by removal of Eosin dye from aqueous solution. The results of XRD indicate that the perovskite-type oxide has a good crystal phase at 650 °C. The DTA, XRD, and SEM data revealed that $\text{La}_{0.5}\text{Pb}_{0.5}\text{MnO}_3$ nano particles are prepared successfully via sol–gel modified pechini method. These nanoparticles showed the excellent adsorption efficiency towards Eosin dye in aqueous solution. The adsorption studies were carried out at different pH values, dye concentrations, various adsorbent dosages, and contact time in a batch experiment. The dye removal efficiency was found to be decreased with increasing in initial pH of the dye solution, and nanoadsorbent exhibited good dye removal efficiency at acidic pH specially pH 1. Experimental results indicated that the adsorption kinetic data follow a pseudo-first-order rate for tested dye. The isotherm evaluations revealed that the Freundlich model attained better fits to the experimental equilibrium data than the Langmuir and Temkin models.

Keywords Perovskite-type oxide · Nanopowder · Dye removal · Eosin

Introduction

Textile industry is one of those industries that consume large amounts of water in the manufacturing process [1] and, also, discharge great amounts of effluents with synthetic dyes to the environment causing public concern and legislation problems. Synthetic dyes that make up the majority (60–70 %) of the dyes applied in textile processing industries [2] are considered to be serious health-risk factors. Apart from the aesthetic deterioration of water bodies, many colorants and their breakdown products are toxic to aquatic life [3] and can cause harmful effects to humans [4, 5]. Several physico-chemical and biological methods for dye removal from wastewater have been investigated [6–9] and seem that each technique faces the facts of technical and economical limitations [8].

The traditional physical, chemical and biologic means of wastewater treatment often have little degradation effect on this kind of pollutants. On the contrary, the technology of nanoparticulate photodegradation has been proved to be effective to them. Compared with the other conventional wastewater treatment means, this technology has such advantages as: (1) wide application, especially to the molecule structure-complexed contaminants which cannot be easily degraded by the traditional methods; (2) the nanoparticles itself have no toxicity to the health of our human livings and (3) it demonstrates a strong destructive power to the pollutants and can mineralize the pollutants into CO_2 and H_2O . Due to the excellent features of this technology, it appears promising and has drawn the attention of researchers of at home and abroad [10–12].

Perovskite oxides have caused great interests and have been widely studied for their various properties and application in the recent decades. They can be used as superconductors, and the critical temperature decreases

H. Tavakkoli (✉) · T. Moayedipour
Department of Chemistry, Khuzestan Science and Research
Branch, Islamic Azad University, Ahvaz, Iran
e-mail: htavakkoli59@gmail.com;
h.tavakkoli@khuzestan.srbiau.ac.ir

linearly with increasing A-site disorder, as quantified by the variance in the distribution of A-site cation radii. The critical temperature is also very sensitive to lattice strains [13–16].

In this work, a novel photocatalyst $\text{La}_{0.5}\text{Pb}_{0.5}\text{MnO}_3$ (LPMO) was successfully fabricated through the method of sol–gel in two different temperatures with the aim of enhancing the step of the application of the technology of nanoparticulate proveskites photodegradation. Eosin (Fig. 1) being a typical anionic dye was selected as a model dyeing pollutant to evaluate the removal performance by prepared nanoadsorbent.

Experimental

Synthesis procedure

The perovskite precursor in this work was prepared by the citrate-based sol–gel modified pechini method [17]. Reagents of $\text{La}(\text{NO}_3)_3 \cdot 6\text{H}_2\text{O}$, $\text{C}_6\text{H}_9\text{MnO}_6 \cdot 2\text{H}_2\text{O}$, $\text{Pb}(\text{NO}_3)_2$ and citric acid (99.5 %) were used as starting materials. Then, the aqueous solutions of metal nitrates with nominal atomic ratios $\text{La}:\text{Pb}:\text{Mn} = 0.5:0.5:1$ (LPMO) were mixed together in deionized water. Citric acid was proportionally added to the metal solution to have the same amounts of equivalents. The solution was concentrated by evaporation at approximately 50°C with stirring for 1 h to convert them to stable (La, Pb)/CA complexes. The solution while being stirred was heated at approximately 75°C to remove excess water and subsequently to accelerate polyesterification reaction. Then, the dry gel was obtained by letting the sol into an oven and heated slowly to 120°C . The gel pieces were ground to form a fine powder. Finally, $\text{La}_{0.5}\text{Pb}_{0.5}\text{MnO}_3$ nanoparticles were gained by thermal treatment of the precursor at 650°C for 9 h in air. The

annealing of the amorphous precursor allows removing most of the residual carbon and the hexagonal perovskite phase was obtained.

Characterization

The decomposition and reaction processes of the dried polymeric gel have been analyzed by differential thermal analysis (DTA) and thermogravimetric analysis (TGA) using a STA 503, Germany, in the temperature range from room temperature to $1,000^\circ\text{C}$, in air with a heating rate of $10^\circ\text{C}/\text{min}$. The complex polymeric gel and derived powders have been also analyzed by Fourier transform infrared (FTIR) spectroscopy on Perkin Elmer BX II FTIR spectrometer. The crystallization and microstructure of the oxide powders have been characterized with an X-ray diffractometer employing a scanning rate of 0.02 S^{-1} in a 2θ range from 20 to 70° , using a X pert, 200, Equinox 3000, France, equipped with CuK_α radiation. The data have been analyzed using JCPDS standards. The microstructure and elemental distribution on the surface were investigated using KYKY EM 3200 ($V = 30\text{ kV}$) scanning electron microscopy (SEM) and energy dispersive X-ray spectroscopy (EDX, Inca 400, Oxford Instruments). A UV–Vis spectrophotometer (Perkin Elmer lambda 35) was employed to monitor the residual dye concentration.

Dye removal test

A prepared solution of Eosin was distributed into different flasks (100 ml capacity) and pH was adjusted with the help of the pH meter. Through applying either HCl (0.5 M) or NaOH (0.5 M), the initial pH value of the dye solution was adjusted to the preferred levels. Then, a specified mass of nano-LPMO powder (adsorbent dosage) was added to 10 mL of the Eosin aqueous solution, and the achieved suspension was immediately stirred for a predetermined time. All experiments were conducted at the room temperature. The following are the studied ranges of the experimental variables: pH of solution (1–13), dye concentration (50–250 mg/L), adsorbent dosage (0.005, 0.01 and 0.02) and contact time (1–40 min).

The concentration of the dye in the reaction mixture at different reaction time was monitored by spectrophotometry by measuring the absorption intensity at $\lambda_{\text{max}} = 487\text{ nm}$ with a calibration curve. The removal efficiency of Eosin was defined as follows (1):

$$\text{Removal rate \%} = \frac{C_0 - C_t}{C_0} \times 100 \quad (1)$$

where C_0 is the initial concentration of Eosin and C_t is the concentration of Eosin at certain reaction time t (min).

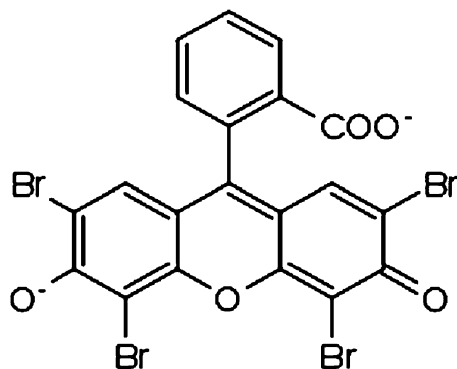


Fig. 1 Molecular structure of Eosin dye

Results and discussion

Thermal analysis

The DTA curve of LPMO is shown in Fig. 2. According to this curve, the exothermic peak at 130 °C can be attributed to the decomposition of the lead citrate into its oxide. The second exothermic peak at 320 °C can be attributed to the decomposition of the manganese citrate into its oxide [18, 19]. The third exothermic peak at 560 °C on this curve may be due to the formation of lanthanum oxide [20, 21].

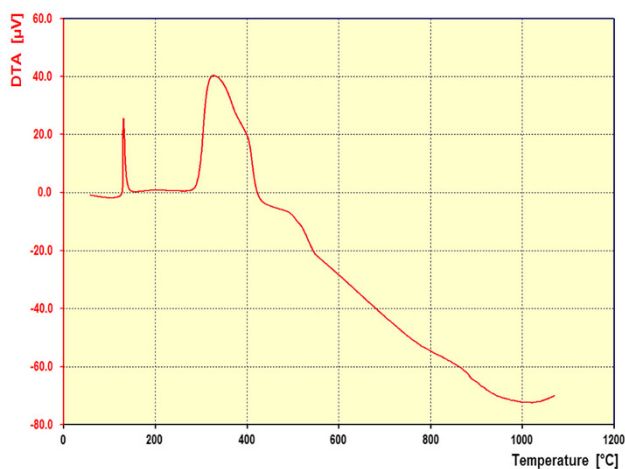


Fig. 2 DTA curve of the LPMO precursors obtained by sol–gel method

Fig. 3 TGA/DTG curves of the LPMO xerogel carried out from room temperature to 1,000 °C in air

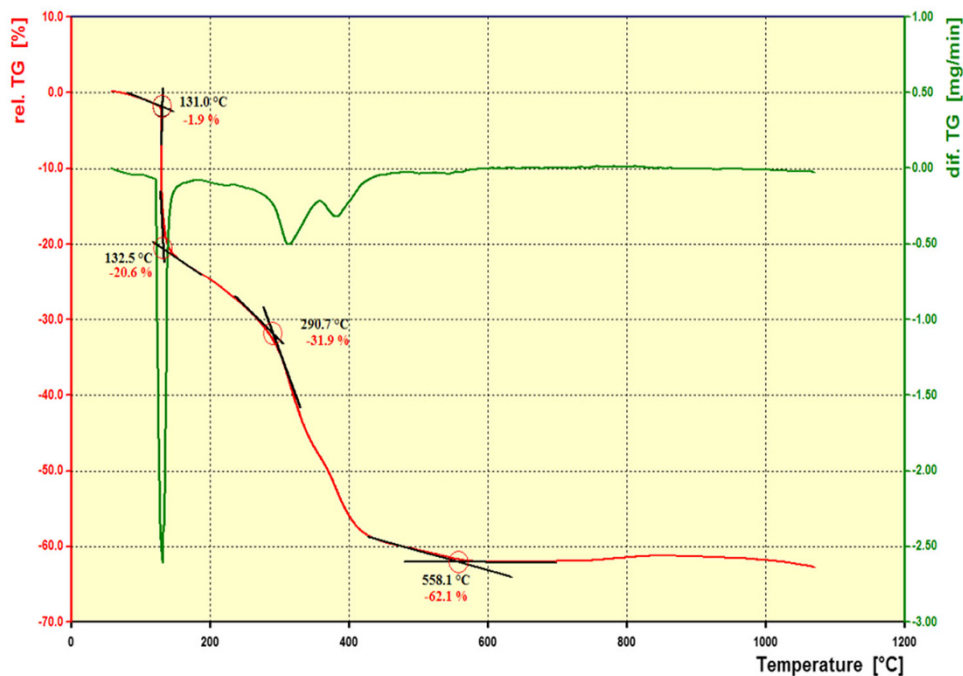


Figure 3 shows TGA curves of the thermal decomposition process of LPMO xerogel obtained at a heating rate of 10 °C/min in the air from room temperature to 1,000 °C. The total weight loss of the xerogel was approximately 62 % and the decomposition process can be divided into two well-established steps. The first weight loss occurs during the heating step from 50 to 290 °C (32 %), which is due to the dehydration and decomposition of nitrates. In this area, DTA curve shows an exothermic peak at 130 °C. A weight loss of about 30 % is observed from 290 °C to around 560 °C, which assigns to the auto-combustion of the nitrate–metal–citric acid followed by the oxidation of evolved gases. The DTA curve reveals a strong exothermic peak at 330 °C which is probable due to the oxidation or combustion of the chelate complex which happens along with forming the metal oxides. Apparently no weight loss was observed above 600 °C. Thus, it is possible to conclude that the optimum calcination temperature is about 650 °C.

X-ray structural analysis

The XRD patterns for the heat-treated LPMO powders are shown in Fig. 4. Sample was heat treated at 650 °C for 9 h (heating rate 3 °C/min) after previously dwelling at 120 °C for 18 h. The XRD results reveal the existence of a perovskite-type phase for sol–gel method at this temperature. As Fig. 4 shows, $\text{La}_{0.5}\text{Pb}_{0.5}\text{MnO}_3$ exhibited a crystalline perovskite phase (ABO_3) with relevant diffraction peaks properly indexed. In this pattern, we can identify the

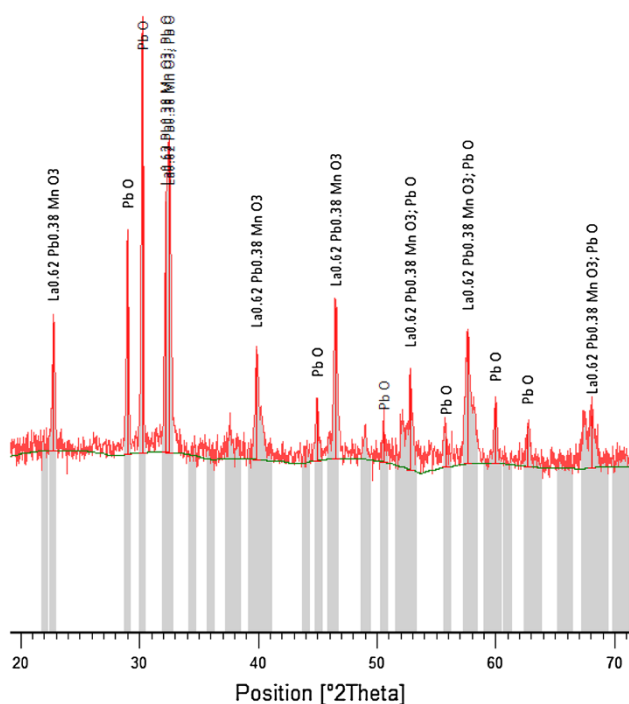
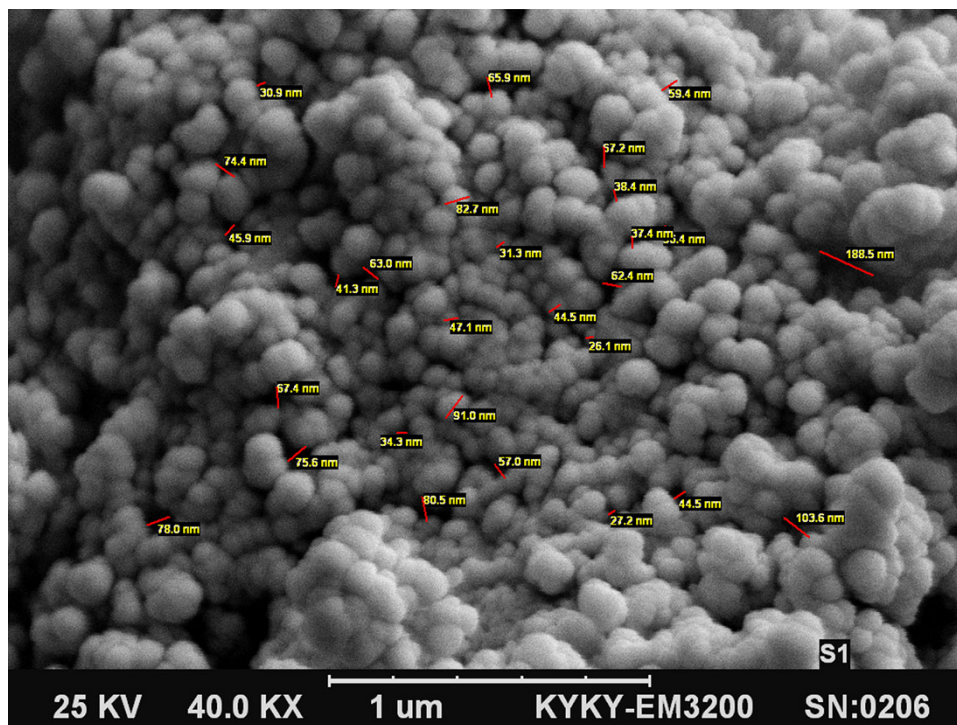


Fig. 4 XRD patterns of samples of the LPMO nanopowder calcinated at 650 °C

presence of (2 0 2), (2 2 0), (4 0 2), (4 0 4), (4 2 4), (4 4 0) and (4 4 5) crystal planes of metallic hexagonal–rhombohedral structure for LPMO (JCPDS-022-1123). At higher temperatures, an increase in the intensity of the crystalline diffraction lines is observed.

Fig. 5 SEM images of LPMO nanopowders



The crystallite grain size of the monophase samples was determined from the full width at half-maximum width (FWHM) of the XRD (2 2 0) peak using the Scherrer's formula (2):

$$D_{hkl} = \frac{0.9\lambda}{\beta_{hkl} \cos \theta_{hkl}} \quad (2)$$

where D_{hkl} is the particle grain size perpendicular to the normal line of ($h k l$) plane, β_{hkl} is the full width at half maximum, θ_{hkl} is the Bragg angle of ($h k l$) peak, and λ is the wavelength of X-ray. The results indicate that LPMO nanopowder sizes calculated at 650 °C are ~39 nm.

SEM images and EDX analysis

The SEM analysis was carried out to determine the morphology of the sample. Figure 5 shows the micrograph of the samples synthesized by the sol–gel modified pechini method and calcinated at 650 °C. According to the SEM images, the porosity of the surface is evident and it appears that the particles have developed with uniform size.

The size of pores varied from 23 to 188 nm. It must be mentioned that catalytic pores of large geometric dimension are more suitable for application to the adsorption process in liquid phase due to the simplicity and easiness in solid–liquid separation and thus with much improved workability for the adsorbent. The surface looks scaly and nearly fully covered with the particles grown on it. Further, it can also be seen from the SEM image that in addition to

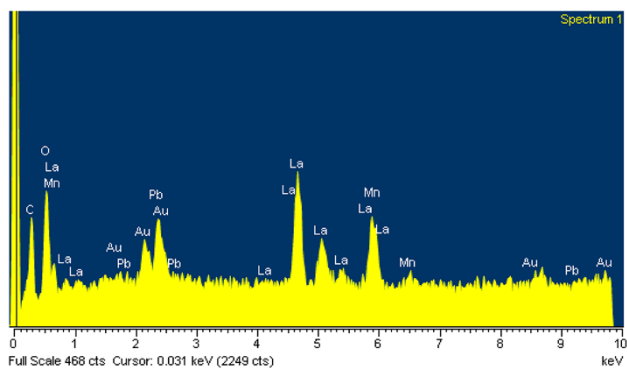


Fig. 6 Energy dispersive X-ray (EDX) spectrum of the LPMO nanoparticles

the larger particles, the surface contains also rather smaller particles. Nonetheless, the dominant particles on the surface were the larger ones. When smaller particles (in the nm range) aggregate, this may lead to the formation of bigger LPMO NPs on the surface.

For further confirmation of the obtained product composition, the EDX analysis was carried out. Figure 6 illustrates EDX spectrum which demonstrates the existence of La, Pb, Mn and O elements in this nanoparticle.

IR spectra

Fourier transform infrared spectra were obtained for xerogels and nanopowder samples after heating treatment

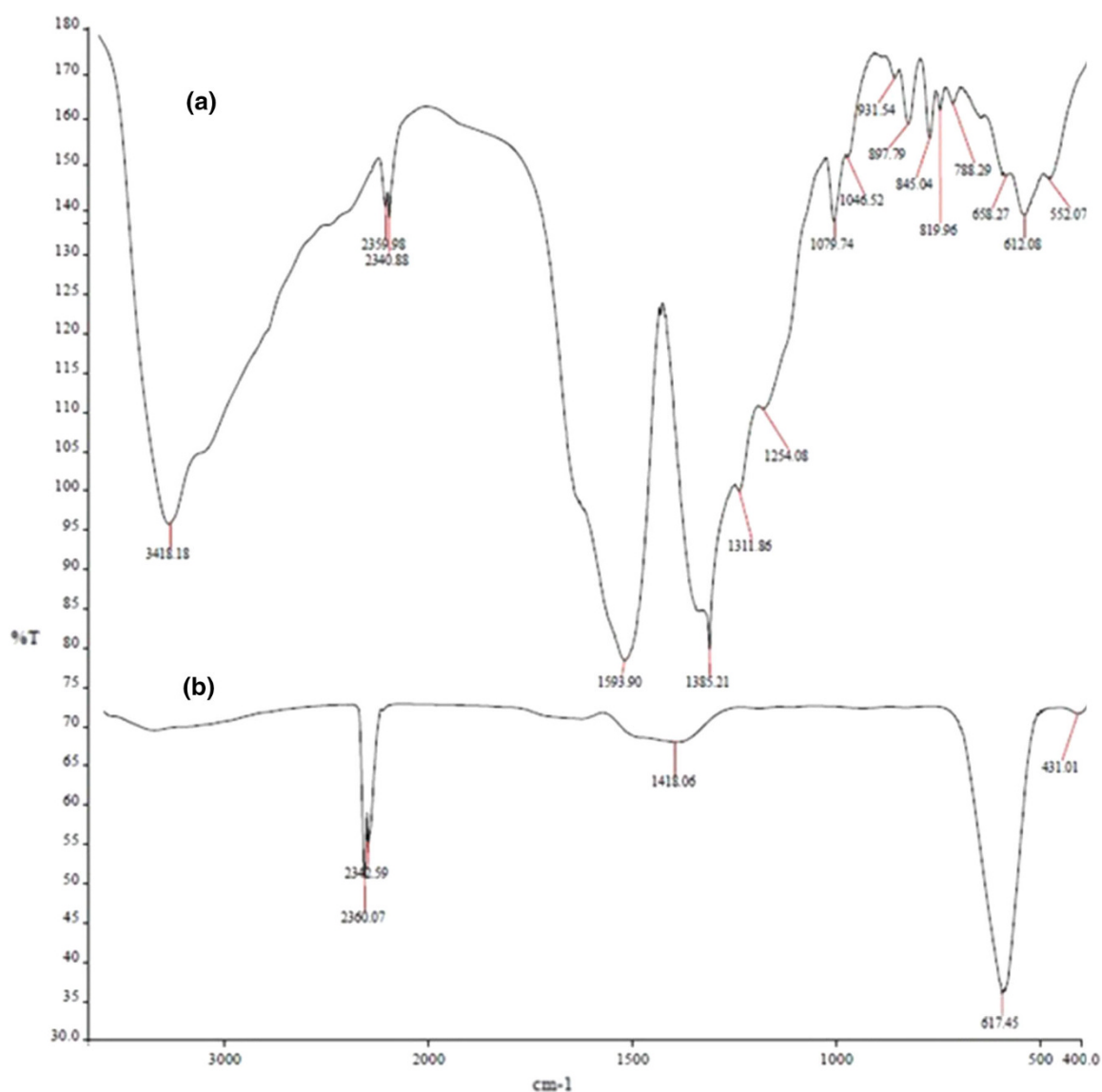


Fig. 7 FT-IR spectra of LPMO xerogel (a), and the calcinated powders at 650 °C (b)

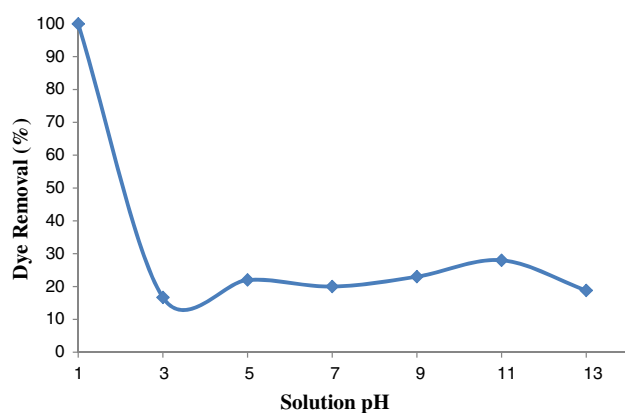


Fig. 8 Effect of initial pH of dye solution on removal of Eosin (LPMO dosage 0.01 g, initial dye concentration 50 mg/L, stirring time 10 min)

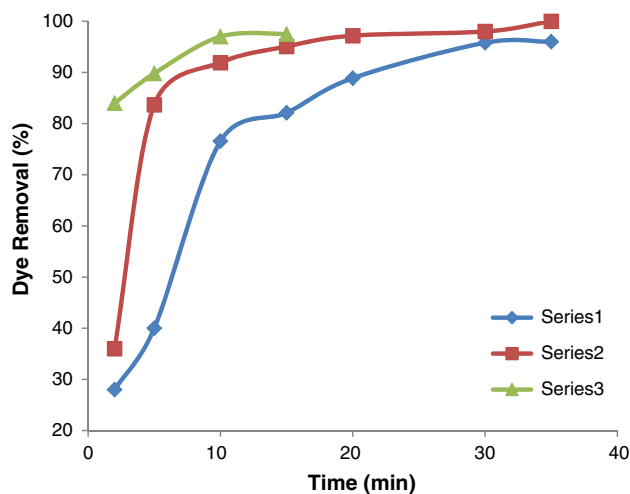


Fig. 9 Effect of stirring time on removal of Eosin in different doses (filled diamond) 0.005 g, (filled square) 0.01 g, (filled triangle) 0.02 g of LPMO (initial dye concentration 50 mg/L, initial pH 1)

leading to the oxides. Figure 7a, b shows the FTIR spectra of the LPMO powders in the range of 600–4,000 cm^{-1} , fresh xerogels and calcined at 650 $^{\circ}\text{C}$, respectively. The FTIR spectrum is similar to the most other ABO_3 -type perovskite compounds which have common BO_6 oxygen-octahedral structure [22–24]. Two samples show the typical M–O–C pair vibrations around 1,385 and 1,593 cm^{-1} [25]. The characteristic band at about 1,254 cm^{-1} corresponds to the anti-symmetric NO_3^- stretching vibration [26]. A broad band is observed between 3,400 and 3,500 cm^{-1} which corresponds to the O–H stretching vibration [27] due to water species occluded into the gel. The FTIR spectra of calcined sample show the vanishing of bands related to organic and hydroxyl groups. Two bands are observed at 400–650 cm^{-1} in the FTIR spectrum of sample, one of them is strong at $\sim 617 \text{ cm}^{-1}$ and other

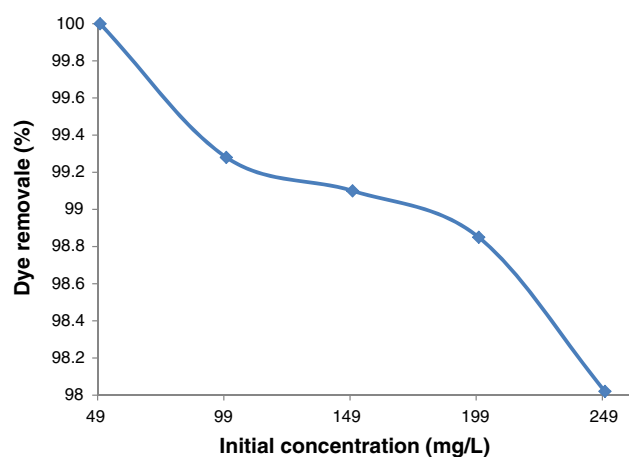


Fig. 10 Effect of initial dye concentration on removal of Eosin (LPMO dosage 0.01 g, initial pH 1, stirring time 20 min)

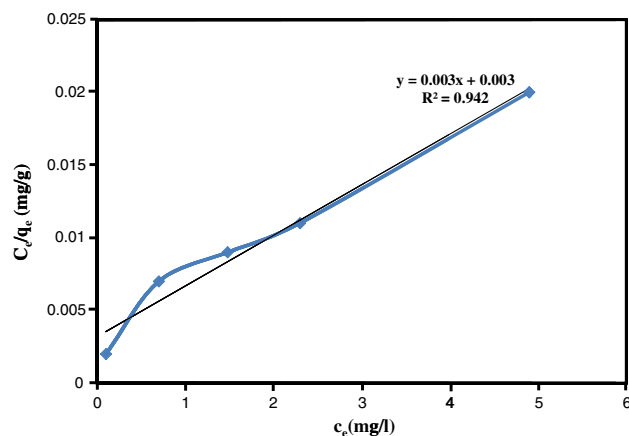


Fig. 11 Langmuir isotherm plot of Eosin adsorption onto LPMO nanoparticles: LPMO dosage 0.01 g, initial pH 1, stirring time 20 min, initial dye concentration 50, 100, 150, 200, 250 mg/L

weak peaks at 431 cm^{-1} . These peaks are characteristics of perovskite oxides and can be attributed to ν M–O stretching and δ O–M–O bending mode of vibrations, respectively [28, 29].

Adsorption study

Effect of pH

The pH of the dye solution can play an important role in the whole adsorption process. To determine the effect of the initial solution pH on the dye removal efficiency of Eosin by LPMO particles, pH values are changed from 1 to 13, with a fixed initial concentration of dye (50 mg/L), contact time (10 min) and adsorbent dosage (0.01 g).

As Fig. 8 shows, the dye removal was much bigger in acidic pH (pH 1 and 2), and it declined when the pH



was increased from 3 to 13. Due to the fact that the Eosin removal rose to its maximum value at pH 1 (the removal of Eosin above 98 % was attained), the dominant adsorption mechanism might be the electrostatic attraction between the dye molecules (negatively charged) and LPMO surface (positively charged). Thus, to reach the optimized condition to remove Eosin, acidic pH should be used and pH 1 seems to give rise to the best result. That is why this pH was selected for the next experiments.

Effect of contact time and adsorbent dosage

To further assessing of dye removal, the effects of mixing time and adsorbent dosage on the removal of Eosin by LPMO nanoparticles were studied. Initial dye concentrations and pH of the solutions were fixed at 50 mg/L and 1, respectively, for all the batch experiments.

As it is obvious, Fig. 9, the increase in mixing time in different dosages of adsorbent leads to a decrease in the concentration of Eosin. This behavior also occurred when adsorbent dosage increased from 0.005 to 0.02 g. This decrease in the concentration is because of the adsorption of Eosin on LPMO nanoparticles and also due to the greater number of adsorption sites for dye molecules made available at greater LPMO dosages. The removal efficiency of Eosin at the initial dosage of 0.005 g grew from 28 % at the second minute of contact to 95 % at the 40th minute. However, with increasing LPMO dosage to 0.02 g, the percentage of removal obtained in the second minute of stirring was 84 %, and complete removal (99 %) was achieved when the stirring was continued till time equals to 15 min. The low adsorbent dosage used for complete removal of Eosin on to LPMO nanopowder is an advantage of this study.

Effect of dye concentration

Another significant variable that can influence the adsorption process is the initial dye concentration. The effect of initial Eosin concentration on dye removal percentage by LPMO particles was investigated by changing the initial dye concentration from 50 to 250 mg/L at pH 1, an adsorbent dosage of 0.02 g and contact time of 10 min, as illustrated in Fig. 10. Results reveal that decolorization of textile dye Eosin decreases with the rise in initial concentration. As can be seen, when the concentration was increased to 250 mg/L, the removal percentage decreased from around 100 % at a concentration of 50 mg/L to 98 %. This behavior shows the dependency of adsorption to initial concentration of Eosin, although the appropriate efficiency of adsorbent maintains in high concentrations.

Adsorption kinetics

Several models are available to investigate the adsorption kinetics. The first- (Eq. 3) and second (Eq. 4)-order reaction rate equations are the most commonly applied models [30, 31]. To find a suitable chemical removal model for describing the experimental kinetic data, the data were fitted into the first- and second-order models:

$$\ln C(t) = \ln C_0 - k_1 t \quad (3)$$

$$\frac{1}{C(t)} = k_2 t + \frac{1}{C_0} \quad (4)$$

where k_1 and k_2 are the first-order and second-order rate constants, respectively. The plots of experimental results of the two models showed that the removal of dye follows first-order kinetics with rate constant of $0.105 \text{ M}^{-1} \text{ min}^{-1}$.

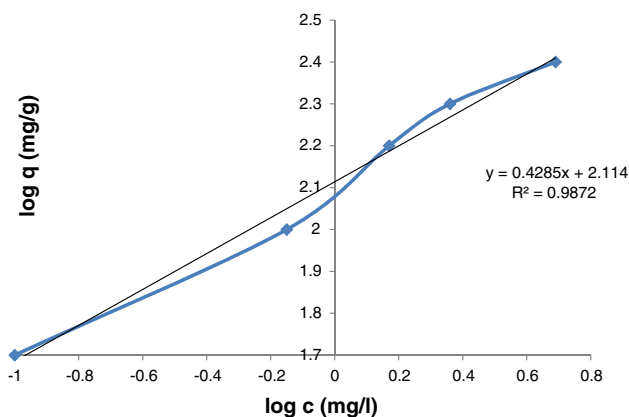


Fig. 12 Freundlich isotherm plot of Eosin adsorption onto LPMO nanoparticles: LPMO dosage 0.01 g, initial pH 1, stirring time 20 min, initial dye concentration 50, 100, 150, 200, 250 mg/L

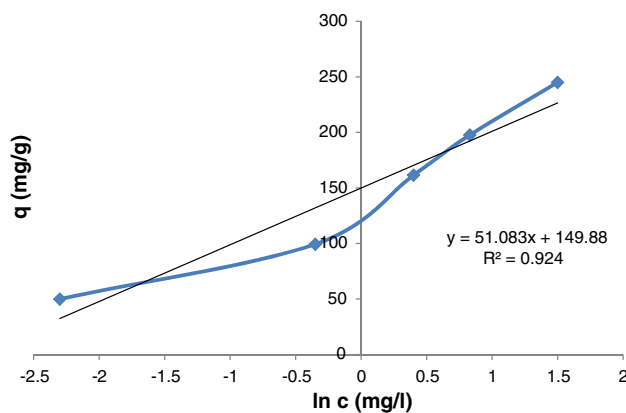


Fig. 13 Temkin isotherm plot of Eosin adsorption onto LPMO nanoparticles: LPMO dosage 0.01 g, initial pH 1, stirring time 20 min, initial dye concentration 50, 100, 150, 200, 250 mg/L

Table 1 Isotherm constants for Eosin adsorption on LPMO nanoparticles

Adsorbent La _{0.5} Pb _{0.5} MnO ₃	Langmuir model		Freundlich model		Temkin model	
	q_{\max} (mg g ⁻¹)	b (L mg ⁻¹)	K_F (mg ^{1-1/n} L ^{1/n} g ⁻¹)	n	A_T (L/g)	B_T (J/mol)
	33.3	10.01	125.89	2.33	18.17	0.162

Adsorption isotherms

The quantity of the dye that could be adsorbed over the nanoperovskites surface is a function of concentration and may be explained by adsorption isotherms. The Langmuir, Freundlich and Temkin isotherm models were applied to the adsorption data. For the equilibrium concentration of adsorbate (C_e) and the amount adsorbed at the equilibrium (q_e), the following forms of the Langmuir (Eq. 5) and Freundlich (Eq. 6) adsorption isotherm equations were used (Eqs. 5, 6):

$$\frac{C_e}{q_e} = \frac{1}{K_L q_{\max}} + \frac{C_e}{q_{\max}} \quad (5)$$

$$\log q_e = \log K_F + \frac{1}{n} \log C_e \quad (6)$$

where the q_{\max} (mg g⁻¹) is the surface concentration at mono-layer coverage which illustrates the maximum value of q_e . The b parameter is a coefficient related to the energy of adsorption and it increases with increasing strength of the adsorption bond [32, 33]. K_F and n are constants of the Freundlich equation [34]. The constant K_F represents the capacity of the adsorbent for the adsorbate and n relates to the adsorption distribution.

Moreover, the derivation of the Temkin isotherm assumes that the fall in the heat of adsorption is linear rather than logarithmic, as implied in the Freundlich equation. The Temkin isotherm is as following.

$$q_e = A + B \ln C_e \quad (7)$$

where A and B are isotherm constants.

The linearized form plots of the Langmuir, Freundlich and Temkin isotherms are shown in Figs. 11, 12 and 13. The parameters of these isotherm models for adsorption of Eosin using the La_{0.5}Pb_{0.5}MnO₃ nanoparticles are summarized in Table 1. The value of correlation coefficient for Freundlich isotherm is greater than that of the Langmuir and Temkin isotherms. This indicates that Freundlich model can describe the adsorption of Eosin on nanoperovskites better than the other models.

Conclusions

The nanoperovskite La_{0.5}Pb_{0.5}MnO₃ was prepared by sol-gel method using citric acid. The XRD reveals that the

nanoparticles prepared by calcinating the gel precursor at 650 °C for 4 h have good crystallinity with fine Hexagonal perovskite structure. The FTIR spectroscopy confirmed the structure of obtained nanoperovskites. In the present study, we demonstrated the nanoperovskites can act as a novel adsorbent material for removal of Eosin. The results demonstrated that the Eosin dye can be successfully removed from aqueous solutions by the nanoperovskites. A first-order model describes the adsorption kinetic data. The equilibrium adsorption can be described using Freundlich model. This adsorbent exhibits either comparable or better performance to the existing adsorbents, already reported by researchers for dye removal from aqueous solutions [17, 35, 36]. Therefore, these nanoperovskite-type oxides are promising candidates for the adsorption of different dyes from wastewaters.

Open Access This article is distributed under the terms of the Creative Commons Attribution License which permits any use, distribution, and reproduction in any medium, provided the original author(s) and the source are credited.

References

- Lin, S.H., Chen, M.L.: Treatment of textile wastewater by chemical methods for reuse. *Water Res* **31**, 868–876 (1997)
- Van der Zee, F.P., Bouwman, R.H.M., Strik, D.P., Lettinga, G., Field, J.A.: Application of redox mediators to accelerate the transformation of reactive azo dyes in anaerobic bioreactors. *Biotechnol. Bioeng.* **75**, 691–701 (2001)
- Chung, K.T., Stevens, S.E.J.: Degradation of azo dyes by environmental microorganisms and helminthes. *Environ. Toxicol. Chem.* **12**, 2121–2132 (1993)
- Weisburger, J.H.: Comments on the history and importance of aromatic and heterocyclic amines in public health. *Mutat. Res.* **506**, 9–20 (2002)
- Oliveira, D.P., Carneiro, P.A., Sakagami, M.K., Zanoni, M.V.B., Umbuzeiro, G.A.: Chemical characterization of a dye processing plant effluent—identification of the mutagenic components. *Mutat. Res.* **626**, 135–142 (2007)
- Roosta, M., Ghaedi, M., Shokri, N., Daneshfar, A., Sahraei, R., Asghari, A.: Experimental design based response surface methodology optimization of ultrasonic assisted adsorption of safar-anin O by tin sulfide nanoparticle loaded on activated carbon. *Spectrochim. Acta A* **122**, 223–231 (2014)
- Robinson, T., McMullan, G., Marchant, R., Nigam, P.: Remediation of dyes in textile effluent: a critical review on current treatment technologies with a proposed alternative. *Bioresour. Technol.* **77**, 247–255 (2001)
- Van der Zee, F.P., Villaverde, S.: Combined anaerobic-aerobic treatment of azo dyes—a short review of bioreactor studies. *Water Res.* **39**, 1425–1440 (2005)

9. Roosta, M., Ghaedi, M., Daneshfar, A., Darafarin, S., Sahraei, R., Purkait, M.K.: Simultaneous ultrasound-assisted removal of sunset yellow and erythrosine by ZnS:Ni nanoparticles loaded on activated carbon: optimization by central composite design. *Ultrason. Sonochem.* **21**, 1441–1450 (2014)
10. Pantelis, A.P., Nikolaos, P.X., Dionissios, M.: Treatment of textile dyehouse wastewater by TiO₂ photocatalysis. *Water Res.* **40**, 1276–1286 (2006)
11. Arana, J., Herrera Melian, J.A., Herrera Melian, J.A., Dona Rodríguez, J.M., Gonzalez Diaz, O., Viera, A., Perez Pena, J., Marrero Sosa, P.M., Espino Jimenez, V.: TiO₂ photocatalysis as tertiary treatment of naturally treated wastewater. *Catal. Today.* **76**, 279–289 (2002)
12. Mansilla, H.D., Bravo, C., Ferreyra, R., Litter, M.I., Jardim, W.F., Lizama, C., Freer, J., Fernandez, J.: Photocatalytic EDTA degradation on suspended and immobilized TiO₂. *J. Photochem. Photobiol. A. Chem.* **181**, 188–194 (2006)
13. Meadowcroft, D.B.: Low-cost oxygen electrode material. *Nature* **226**, 847–848 (1970)
14. Zhu, Y., Tan, R., Yi, T., Ji, S., Ye, X., Cao, L.: *J. Mater. Sci.* **35**(21), 5415 (2000)
15. Yongfa, Z., Ruiqin, T., Tao, Y., Song, G., Chunhua, Y., Lili, C.: Preparation of nanosized La₂CuO₄ perovskite oxide using an amorphous heteronuclear complex as a precursor at low-temperature. *J. Alloys Comp.* **311**, 16–21 (2000)
16. De La Cruz, E.M.G., Falcon, H., Pena, M.A., Fierro, J.L.G.: Role of bulk and surface structures of La_{1-x}Sr_xNiO₃ perovskite-type oxides in methane combustion. *Appl. Catal. B Environ.* **33**, 45–55 (2001)
17. Yazdanbakhsh, M., Tavakkoli, H., Hosseini, S.M.: Characterization and evaluation catalytic efficiency of La_{0.5}Ca_{0.5}NiO₃ nanopowders in removal of reactive blue 5 from aqueous solution. *Desalination* **281**, 388–395 (2011)
18. Kao, C.F., Jeng, C.L.: Preparation and characterization of lanthanum nickel oxides by combined coprecipitation and molten salt reactions. *Ceram. Int.* **25**, 375–382 (1999)
19. Kao, C.F., Jeng, C.L.: Preparation and characterisation of lanthanum nickel strontium oxides by combined coprecipitation and molten salt reactions. *Ceram. Int.* **26**, 237–243 (2000)
20. Neumann, A., Walter, D.: The thermal transformation from lanthanum hydroxide to lanthanum hydroxide oxide. *Thermochim. Acta* **445**, 200–204 (2006)
21. Mazlounia, M., Shahcheraghia, N., Kajbafvala, A., Zanganeha, S., Laka, A., Mohajerania, M.S., Sadrnezhad, S.K.: 3D bundles of self-assembled lanthanum hydroxide nanorods via a rapid microwave-assisted route. *J. Alloys Compd.* **473**, 283–287 (2009)
22. Leite, E.R., Sousa, C.M.G., Longo, E., Varela, J.A.: Influence of polymerization on the synthesis of SrTiO₃: part I. characteristics of the polymeric precursors and their thermal decomposition. *Ceram. Int.* **21**, 143–152 (1995)
23. Nimmo, W., Ali, N.J., Brydson, R.M., Calvert, C., Hampartsoumian, E., Hind, D., Milne, S.J.: Formation of lead zirconate titanate powders by spray pyrolysis. *J. Am. Ceram. Soc.* **86**, 1474–1480 (2003)
24. Sakar-Deliormanli, A., Celik, E., Polat, M.: Solubility and aging of lead magnesium niobate in water. *Ceram. Int.* **35**, 503–508 (2009)
25. Kim, J., Honma, I.: Synthesis and proton conducting properties of zirconia bridged hydrocarbon/phosphotungstic acid hybrid materials. *Electrochim. Acta* **49**, 3179–3183 (2004)
26. Liu, S., Qian, X., Xiao, J.: Synthesis and characterization of La_{0.8}Sr_{0.2}Co_{0.5}Fe_{0.5}O_{3±δ} nanopowders by microwave assisted sol–gel route. *J. Sol-Gel. Sci. Technol.* **44**, 187–193 (2007)
27. Kuznetsov, P.N., Kuznetzova, L.I., Zhyzhaev, A.M., Pashkov, G.L., Boldyrev, V.V.: Ultra fast synthesis of metastable tetragonal zirconia by means of mechanochemical activation. *Appl. Catal. A* **227**, 299–307 (2002)
28. Singh, R.N., Lal, B.: High surface area lanthanum cobaltate and its A and B sites substituted derivatives for electrocatalysis of O₂ evolution in alkaline solution. *Int. J. Hydrogen Energy* **27**, 45–55 (2000)
29. Hao, Y., Li, J., Yang, X., Wang, X., Lu, L.: Preparation of ZrO₂–Al₂O₃ composite membranes by sol–gel process and their characterization. *Mater. Sci. Eng. A* **367**, 243–247 (2004)
30. Hsueh, C.L., Lu, Y.W., Hung, C.C., Huang, Y.H., Chen, C.Y.: Adsorption kinetic, thermodynamic and desorption studies of Reactive Black 5 on a novel photoassisted Fenton catalyst. *Dyes Pigm.* **75**, 130–135 (2007)
31. Indra, D.M., Vimal, C.S., Nitin, K.A.: Removal of orange-G and methyl violet dyes by adsorption onto bagasse fly ash—kinetic study and equilibrium isotherm analyses. *Dyes Pigm.* **69**, 210–223 (2006)
32. Kritikos, D.E., Xekoukoulotakis, N.P., Psillakis, E., Mantzavinos, D.: Photocatalytic degradation of reactive black 5 in aqueous solutions: effect of operating conditions and coupling with ultrasound irradiation. *Water Res.* **41**, 2236–2246 (2007)
33. Langmuir, I.: The adsorption of gases on plane surfaces of glass, mica and platinum. *J. Am. Chem. Soc.* **40**, 1361–1403 (1918)
34. Freundlich, H.M.F.: Over the adsorption in solution. *Z. Phys. Chem. A* **57**, 385–471 (1906)
35. Belhachemi, M., Addoun, F.: Adsorption of congo red onto activated carbons having different surface properties: studies of kinetics and adsorption equilibrium. *Desalin. Water Treat.* **37**, 122–129 (2012)
36. Cheng Shih, M.: Kinetics of the batch adsorption of methylene blue from aqueous solutions onto rice husk: effect of acid modified process and dye concentration. *Desalin. Water Treat.* **37**, 200–214 (2012)

